Aerogel Spring-Back Correlates with Strain Recovery: Effect of Silica Concentration and Aging

Deeptanshu Sivaraman,* Shanyu Zhao, Subramaniam Iswar, Marco Lattuada, and Wim J. Malfait

Silica aerogels display exceptional properties and great application potential, with a mature market in thermal insulation. Both supercritical drying (SCD) and ambient pressure drying (APD) routes are implemented industrially. Herein, how aging and silica content affect the mechanical properties, and how these in turn determine the shrinkage, spring back, and density during APD are systematically investigated. The APD densities display a U-shaped dependence of density w.r.t. silica concentration. At low silica concentrations, the gels cannot withstand the capillary forces during APD and dense xerogels are obtained. At intermediate to high concentrations, APD shrinkage is strongly reduced and density increases with silica concentration. A series of cylinders are prepared by SCD and investigated by uniaxial compression and their strain recovery is determined systematically. The mechanical responses are plastic, viscoelastic, and brittle in nature for low, intermediate, and high silica concentrations, respectively. The strain recovery of the SCD cylinders correlates to the degree of spring back during APD. The viscoelastic response of SCD aerogels having 6 wt% corresponds to the silica concentration where a minimum in APD aerogel density is observed. The importance of gel mechanics for silica aerogel spring back during APD, in addition to surface modification and hydrophobization is highlighted.

1. Introduction

Silica aerogels are mesoporous structures composed of a particle network surrounding mesopores (2–50 nm diameter). Their porosity contributes 80–99% to the high mesoporous volume, along with the tortuosity of the skeleton backbone, lend aerogels their exceptional properties: densities ranging from 0.004 to 0.500 g cm^{-3}, high specific surface areas (600–1200 m^2 g^{-1}), and ultralow thermal conductivities (down to 12–15 mW m^{-1} K^{-1}).[1] These properties open up a wide array of use-cases in fields such as thermal insulation,[2–4] catalysis,[5] and drug delivery.[6] In the current market, silica aerogel is almost exclusively used for thermal insulation (industrial, pipelines, and buildings).[3] Other applications such as in electronic devices,[7] Knudsen pumps,[8] solar panels,[9] waste adsorbents and sensors,[10–12] whereas other, nonsilica-based aerogel materials, are mostly not market ready, but in the academic research or early technology transfer stage.

The traditional preparation of silica aerogels involves several steps: gelation of silica precursors (SPs) such as waterglass, ion-exchanged waterglass, or silicon alkoxides (e.g., tetraethyl orthosilicate TEOS), followed by aging,[13] hydrophobization,[14] and solvent exchange and supercritical drying (SCD).[15] The bottlenecks preventing large-scale production and application are related to the poor mechanical properties and, arguably more importantly, cost. Significant efforts have been dedicated to reinforce silica aerogels with a wide range of strategies, including surface crosslinking[16–18] (nano)fiber reinforcement,[19] composites,[20,21] and foam impregnation,[22] and the use of organosiloxane precursors.[23–26] The high cost of silica aerogel is related to the high cost of raw materials (SPs and hydrophobization agents), the large volumes of solvents that need to be processed and recycled,[27] and the high production cost due to the SCD process.[28] The SCD barrier can be circumvented by ambient pressure drying (APD), which reduces cost and complexity through a simple evaporative drying process. APD may also increase process safety and scalability for aerogel production.[29]

Evaporative drying, however, is not an easy feat. For silica aerogels, an envelope density of 0.120 g cm^{-3} provides the optimal, lowest thermal conductivity[1,20] and this is the target density for APD. However, the small pore sizes lead to very strong capillary forces at the solvent–vapor interface and these forces induce permanent pore collapse and shrinkage, leading to dense xerogels, rather than low-to-intermediate density aerogels. Aerogel

D. Sivaraman, S. Zhao, S. Iswar, W. J. Malfait
Laboratory for Building Energy Materials and Components
Swiss Federal Laboratories for Materials Science and Technology
Empa, Überlandstrasse 129, 8600 Dübendorf, Switzerland
E-mail: deeptanshu.sivaraman@empa.ch

D. Sivaraman, M. Lattuada
Department of Chemistry
University of Fribourg
Av. de l'Europe 20, 1700 Fribourg, Switzerland

The ORCID identification number(s) for the author(s) of this article can be found under https://doi.org/10.1002/adem.202100376

spring back can reverse this shrinkage through the recovery of (nearly) the original volume toward the end of the drying process, but only occurs when specific conditions are fulfilled, most notably a sufficient hydrophobization of the silica surfaces and a sufficient mechanical strength. Although it is possible to produce large monolithic organosilica aerogel pieces by APD under some specific conditions,[25][26] the industrially most relevant APD processes target the production of silica aerogel granulate or powder.

The importance of hydrophobization for APD is well documented. In fact, the breakthrough of evaporative drying was only made possible with the development of surface silylation.[30–32] Unmodified silica gel surfaces are covered with silanol ($\equiv$Si—OH) and/or (m)ethoxy groups (e.g., $\equiv$Si—OR with R=methyl, ethyl) that are prone to water and/or alcohol condensation during drying. The newly formed siloxane bridges ($\equiv$Si—O—Si$\equiv$) lock in the shrunken state and prevent spring back when capillary forces are removed at the end of the drying process. The hydrophobization treatment converts a large fraction of these reactive silanol and alkoxy groups into unreactive, hydrophobic groups, most often trimethylsilyl ($\equiv$Si—O—Si(CH$_3$)). The hydrophobization step not only is a critical requirement to enable APD, but also renders the final aerogel hydrophobic, which is an essential benefit for most applications. Because of its importance, silica aerogel hydrophobization has been researched thoroughly in terms of hydrophobization agents,[30,31,33] surface modification strategies,[11,34,35] and analytics.[33,36]

The second requirement to enable APD is an appropriate mechanical response of the gels during/after drying. The importance of gel aging toward gel mechanics and APD has been studied in detail. Adequate aging, combined with hydrophobization,[37,38] provides the structure with enough strength for spring back of the aerogel after APD. Aging is a process of increasing the strength of the silica backbone structure by keeping the gel in the gelation liquid, or a specially prepared aging solution, for an extended duration after gelation, which provides more time for condensation reactions and wider

necks to form between silica particles.[13,38,39] The importance of aging is a known phenomenon, but the exact relationship between silica content, aging, and aerogel mechanics on the one hand, and the spring back effect, on the other hand, have not been explored systematically.

In this study, we investigate the interplay between mechanical properties of SCD aerogels and the spring back effect in APD materials, with a focus on compression rather than bending experiments,[40] because axial forces are predominant during the drying process.[39,41] Cylinders prepared with SCD are subjected to uniaxial compression–decompression tests to quantify the strain recovery as a function of silica concentration, aging time, and maximum strain. The mechanical data are then compared with the degree of shrinkage and permanent densification and degree of spring back of APD aerogel granulate prepared under the same conditions. Our data highlight is the first-order control of silica concentration on mechanical properties, strain recovery, and aerogel spring back.

2. Results

2.1. Sample Appearance

The APD samples collapse into smaller millimeter-sized pieces during the drying process, whereas the SCD aerogels are recovered as pristine monoliths, consistent with the presence and absence of capillary forces during drying.[42] The recovered SCD samples after compression to, and decompression from 40% strain (**Figure 1**) provide a first qualitative illustration of the change in mechanical response for different silica concentrations: plastic (4 wt%), viscoelastic (6 wt%), and brittle (8 wt%). Both the APD and SCD samples display the optical translucency and blue hues typical of silica aerogel. This transparency tends to increase with increasing silica concentration (and therefore its density), similar to reports by Wong et al.[43] and presumably due to the reduction in pore size.[42,44]
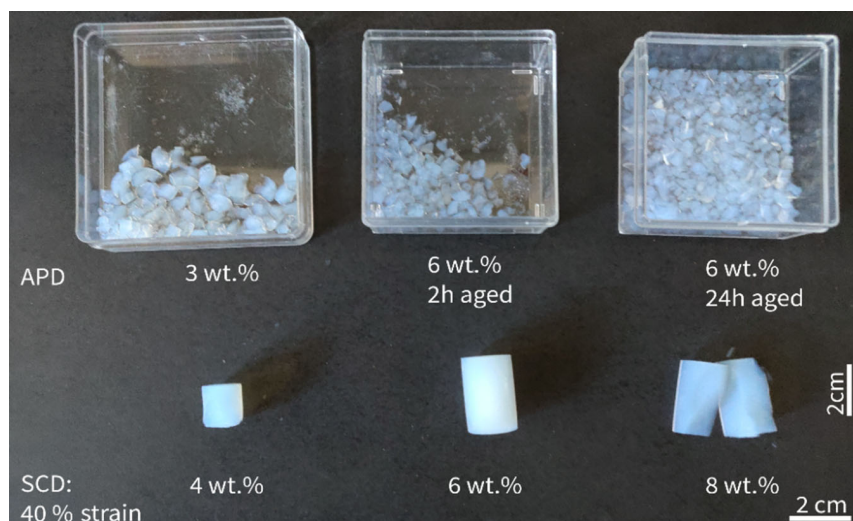

Figure 1. APD and SCD samples from different silica aerogel concentrations (sets 1, 2, and 24 h aging). The depicted SCD cylinders have been compressed–decompressed up to 40% strain.

2.2. Nitrogen sorption, SEM, and Microstructure

The silica aerogels in this study display Brunauer–Emmett–Teller (BET) surface areas[45] between 784 and 988 $m^2 g^{-1}$ (**Table 1**) and type IV sorption isotherms (**Figure 2**), both typical for silica aerogels.[46][47] The Barrett–Joyner–Halenda (BJH) pore volumes and diameters[48,49] are also shown in Table 1, in addition to those calculated from density assuming cylindrical pores (Section 2.3). As is typical for silica aerogels, the BJH pore volumes and BJH pore diameters are smaller than those calculated from density, due to the inability of nitrogen sorption to sample larger pores (>50 nm), the possible deformation of silica aerogel during nitrogen sorption, the limitations of the BJH model, or a combination of these factors.[50] For the SCD aerogels, the calculated pore volume and average diameter display the expected monotonic decrease as a function of sol silica concentration and aerogel density. The BJH pore volume and pore diameters display a more complex dependence on density (Table 1, Figure 2b), but this complexity may be due to the complex interplay between the actual pore size distribution and the density-dependent sample deformation during nitrogen sorption analysis, rather than true variations in mesopore volume.

All investigated silica aerogels, both SCD and APD, display the microstructures expected for silica aerogel, with connected dumbbell, pearl-necklace structures of (secondary) silica nanoparticles around the mesopores (**Figure 3**).[18,36] The solid fraction increases (with the silica concentration and density), and the apparent pore size decreases. For differently aged samples, there is no discernable difference in the SEM images.

2.3. Effect of Aging and Concentration on Aerogel Density

The variation of the APD density with aging time and silica concentration is a result of the interplay between mass loading and the partial pore collapse and shrinkage during APD, which is known to be affected by aging.[38][51] The density of the SCD aerogels increases monotonically with increasing silica concentration (**Table 2**), but this is not the case for APD aerogels, where we see a minimum in density at 6 wt% of silica in the sol. At this silica concentration, the APD density of the 2 h-aged aerogel is higher than that of the 24 h-aged aerogel.

The samples from set 2 provide a more detailed, systematic picture into the interplay between silica concentration and aging on the one hand and APD aerogel density on the other (**Figure 4**). The shrinkage during APD, approximated by the ρ_{APD}/ρ_{SCD} ratio, is small and independent of aging time at high sol silica concentrations (>8 wt%), with ρ_{APD}/ρ_{SCD} ratios close to 1 for all aging times (Figure 4a). At intermediate sol silica concentration (6–8 wt%), the APD shrinkage strongly depends on aging time: low shrinkage for long aging times, high shrinkage for

Table 1. Nitrogen sorption model results for various silica concentrations (set 1, SCD unless indicated otherwise).

Silica [wt%]	ρ[a)] [g cm^{-3}]	Aging time [h]	S_{BET} [m^2 g^{-1}]	V_{pore} BJH [cm^3 g^{-1}]	D_{pore} BJH [nm]	V_{pore} calc. [cm^3 g^{-1}]	D_{pore} calc. [nm]
4	0.073	24	909	4.1	18	13	58
6	0.104	2	889	2.5	14	9.1	39
8	0.137	24	988	6.3	28	6.8	28
12	0.185	24	805	3.1	14	4.9	24
6 (APD)	0.142	2	784	3	14	6.5	29

[a)]Uncertainty of ≈5% relative. Envelope density reported.
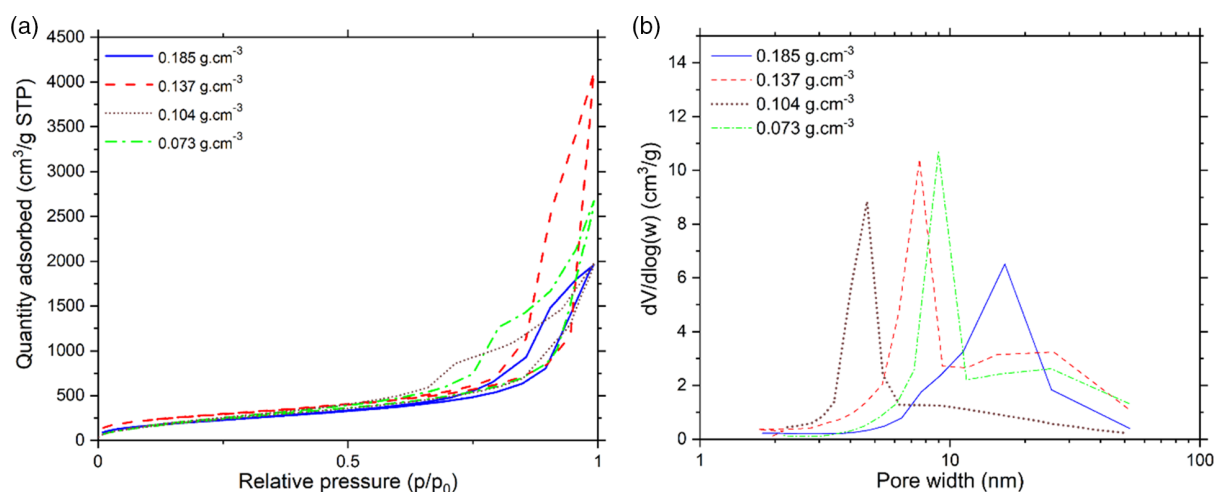

Figure 2. a) Adsorption–desorption isotherms and b) BJH–desorption curves of pore width against differential pore volume for SCD aerogels with different densities (Set 1).
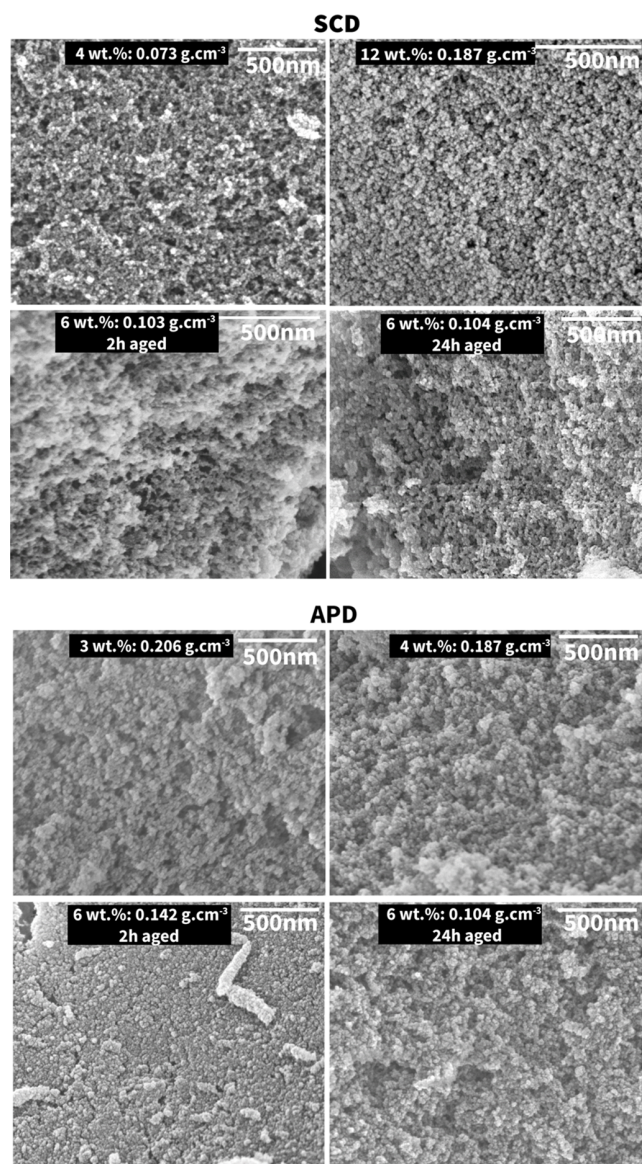
Figure 3. SEM images of aerogels prepared with different silica concentrations and aging times (set 1).

Table 2. Aerogel density (set 1).

Silica [wt%]	Aging time [h]	ρ_{SCD} [g cm^{-3}]	ρ_{APD} [g cm^{-3}]
3	24	0.067	0.206
4	24	0.073	0.187
5	24	0.090	0.218
6	2	0.103	0.142
6	24	0.104	0.114
8	24	0.137	0.137[a]
12	24	–	0.239[a]

[a]Samples from set 2.

short aging times. At the lowest sol silica concentration, the APD shrinkage also decreases with increasing aging time, but the ρ_{APD}/ρ_{SCD} ratio remains far above 1, even for the longest aging time.

The complex concentration and aging dependence of APD shrinkage (Figure 4a), combined with the variations in mass loading due to different silica concentrations, results in a U- or V-shaped dependence of APD aerogel density on silica concentration (Figure 4b), with a minimum in APD aerogel density at intermediate silica concentrations. At low silica concentrations, the excessive APD shrinkage leads to higher densities, whereas the reduce shrinkage at high silica concentrations cannot offset the effects of increased solid content at high silica concentrations. The minimum in density shifts to lower densities and lower sol silica concentrations when longer aging times are applied because of the reduced APD shrinkage. In contrast to the complex APD density variations, the SCD densities are a simple function of silica concentration and the values approach the theoretical density, calculated from the silica concentration, multiplied by a factor of 1.34 to account for the mass of the TMS groups grafted during hydrophobization.[36] The residual difference is related to a minor degree of shrinkage during aging and/or SCD.

In summary, the density data indicate that the following conditions need to be fulfilled to produce by APD silica aerogels with densities that approach those of their SCD counterparts: either a high silica concentration in the sol, in which case the aging time and conditions are not important, or an intermediate silica concentration, combined with sufficiently long aging times. No APD aerogels with low to intermediate density can be produced from very dilute silica sols.

2.4. Uniaxial Compression and Strain Recovery

In this section, we evaluate the mechanical properties of silica aerogel cylinders, prepared by SCD, as a function of aerogel density and aging time. We focus on the strain recovery after uniaxial compression to different values of maximum strain. The results from Section 2.4 will then be correlated to the spring back phenomena described earlier (Section 2.3) in Section 2.5.

2.4.1. Maximum Strain: Compressible, Viscoelastic and Brittle Aerogels

Figure 5 shows the fracture strain of the samples that fractured (broken, cracked, or crushed) during the uniaxial compression tests. The data display a wide range in fracture strain for a given density due to sample imperfections that can occur in any of the aerogel production and processing stages, leading to chipping, internal cracks, or nonplanar surfaces. Nevertheless, the maximum fracture strain for a given density provides an estimate of maximum limit of compressive strain a particular density can sustain for a defect-free sample. Lower-density aerogels, up to 0.075 g cm^{-3} are highly compressible with high maximum fracture strain values. The samples are not brittle and generally can be recovered as intact cylinders or disks after the experiment. The high maximum strains are possibly related to the stretchability of the matrix network,[52] and/or could be due to longer aspect
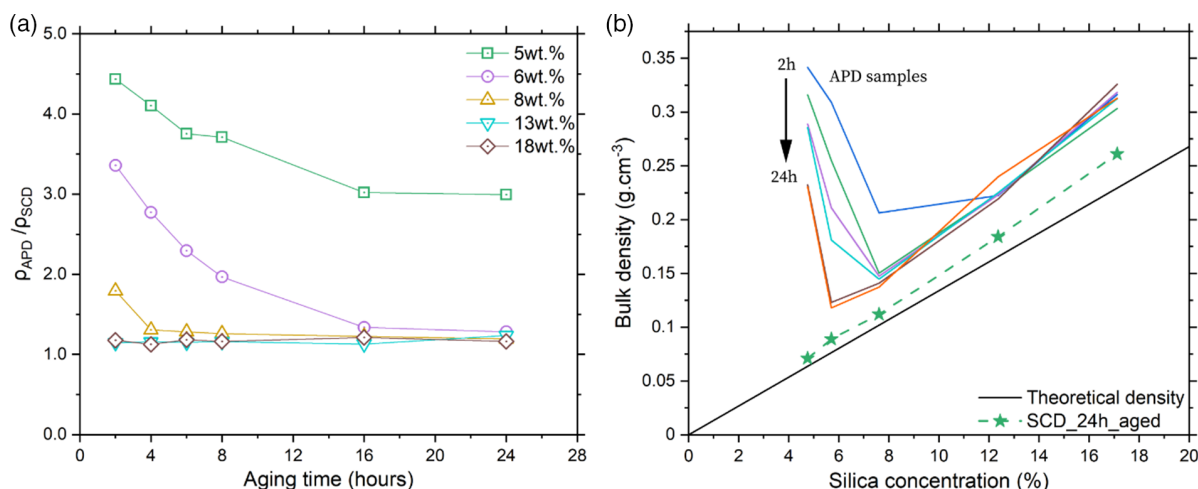
Figure 4. a) APD shrinkage, approximated by ρ_{APD}/ρ_{SCD}, as a function of aging time for different sol silica concentrations (set 2). b) Envelope density as a function of silica concentration for differently aged silica aerogels (set 2).
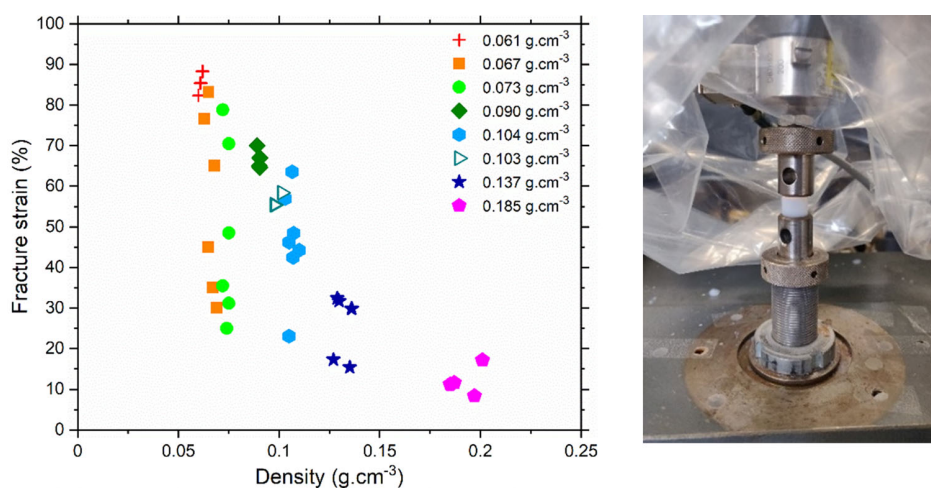

Figure 5. Left: fracture strain as a function of aerogel density (SCD, set 1). Filled markers correspond to 24 h of aging, open triangles correspond to 2 h of aging. Right: compression test done on an aerogel.

ratios for the silica particle chains.[53] Aerogels of intermediate density, 0.075–0.125 g cm^{-3}, display a decrease in maximum fracture strain. In the following sections, we will show that this is the viscoelastic region of operation, where samples can recover their initial dimensions after decompression, typical for the viscoelastic regime. High-density aerogels, >0.125 g cm^{-3}, are brittle with maximum fracture strain values between 10% and 20%.

2.4.2. Compression–Decompression Curves

Figure 6 shows the stress–strain curves of variable density aerogel cylinders that did not fracture during the mechanical testing and could be recovered as pristine disks or cylinders after decompression. All aerogels, irrespective of density, display a classic linear viscoelastic regime at low strains (up to 10%), followed by plastic deformation at higher strain, in agreement with previous observations.[54,55] The compression curves for different

aerogel densities are compared in Figure S1 and S2, Supporting Information.

As expected, lower-density samples (Figure 6a–c) are more compressible, with small slopes in the stress–strain curves at low strain ranges, but the samples can sustain relatively high values of compressive stress without failure (1.5 MPa at ≈80% strain). The decompression curves for these lower density aerogels indicate that most of the strain is irreversible, i.e., the strain values do not return to zero after removal of the mechanical stress. These samples also do not retain their initial height, even after 1 week of test completion. The behavior of low-density silica aerogels is in stark contrast to the general perception of silica aerogels as highly brittle materials.[56]

Aerogels of intermediate density (Figure 6d,e) reach higher compressive stress values for a given strain, but have lower compressive stress at break because of the lower fracture strain (Figure 5). In contrast to the low-density aerogels, most of the deformation is reversible and the samples quickly return to their
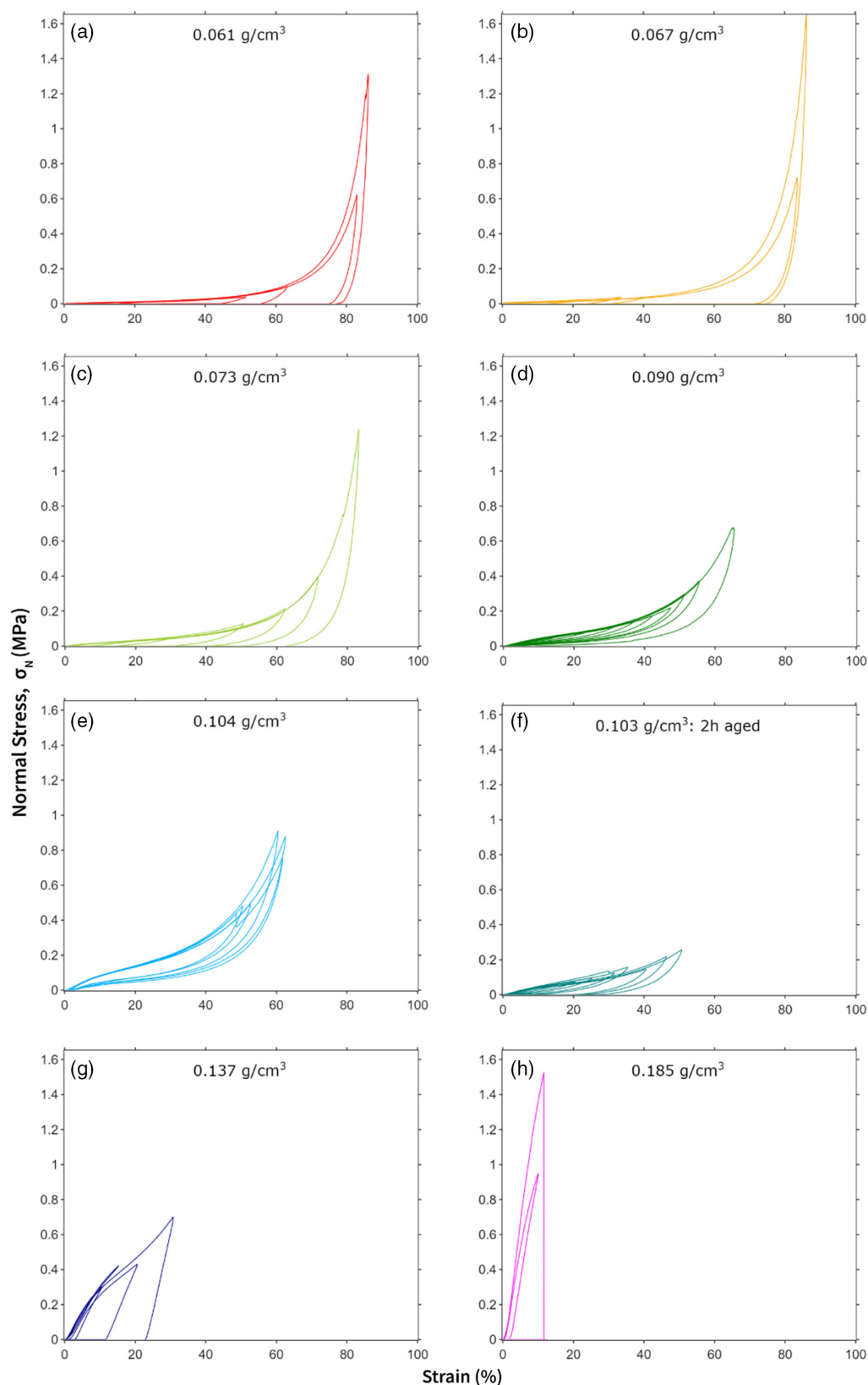
**ADVANCED
SCIENCE NEWS**

www.advancedsciencenews.com

**ADVANCED
ENGINEERING
MATERIALS**

www.aem-journal.com

Figure 6. Uniaxial compression–decompression data for SCD aerogels with variable density (set 1, 24 h aging, f is 2 h aging). The shown densities are binned average densities. Note that, each compression–decompression curve in each subplot corresponds to a unique sample.

**ADVANCED
SCIENCE NEWS**

www.advancedsciencenews.com

**ADVANCED
ENGINEERING
MATERIALS**

www.aem-journal.com

initial dimensions during decompression. This denotes the "reversible compression" region or viscoelastic regime for densities up to around 0.12 g cm^{-3}. Earlier experimental and simulation studies[43,57] had already hinted at the possibility of an "viscoelastic" zone, wherein we see complete strain recovery of the samples after mechanical compression and this is confirmed by our data. A sample that was aged for 2 h instead of the standard 24 h (Figure 6f) shows a mechanical response that is similar to a lower density aerogel, with lower stress values for a given strain, and incomplete stress recovery.

High-density aerogels (Figure 6g,h) have much steeper slopes in the stress–strain curves, but the compressive stress at break values are similar to, not higher than, those of low-density silica aerogels due to the much lower fracture strain, e.g., 1.5 MPa at 12% strain for a 0.185 g cm^{-3} aerogel. The high-density aerogels only partially recover their initial height after decompression. Note that, we cannot directly derive the Poisson's ratio because the diameter of the sample was not monitored throughout the compression tests. In Table S2, Supporting Information, we have listed the apparent Poisson's ratio calculated from the irreversible, postdecompression strain in diameter and height. The values range between small negative values (–0.15) and zero, indicating that there is lateral contraction or no change in the diameters of the samples during uniaxial compression as seen for mordenite framework inverted (MFI) silica zeolites[58] and some cellulose aerogels,[59] respectively.

2.4.3. E-Modulus and σ_x

Even though the focus of this study is on strain recovery, and its correlation to aerogel spring back during APD, the dataset also describes the density and aging dependence of the elastic moduli (E) and σ_{10}, σ_{30}, σ_{50}, and σ_{80} values. The E-moduli display a power–law dependence on aerogel density $E \approx \rho^\alpha$ (**Figure 7**a), typical for silica aerogels,[43,55] alumina aerogels,[60] and biopolymer aerogels.[61] Note that, a single scaling factor α suffices to fit the data over the entire density range, in contrast to the results from early ultrasonic studies that hinted at lower values for the

scaling coefficient at lower density,[62] but consistent with most other available data.[43,63] The value for α derived from the current dataset is 4.3, somewhat higher than the previously reported for silica aerogels, e.g., 3.6[43] and 3.7[63] from experiments or 3.61 from simulations,[64] and significantly higher than what is typical for many other aerogel systems, e.g., 1.75 for alumina aerogels,[60] 1.8 for cellulose aerogels,[61] or 2.7–3.7 for resorcinol–formaldehyde aerogels.[65,66] The E-modulus of the 2 h-aged aerogels is lower by a factor of 1.5–2.5 compared with the 24 h-aged counterparts of similar density, a direct consequence of the formation of thicker interparticle necks during the extended aging time, which increases the structural strength to the aerogel network.[35]

Many industries use secant moduli σ_{10}, σ_{30}, σ_{50}, and σ_{80},[67] i.e., the stress values for a given percentage of strain, rather than E-moduli to describe the sample deformation under stress. Figure 7b shows that the σ_x also display a power–law dependence on aerogel density, similar to the E-moduli, with values for α of 4.36, 4.05, and 3.67 for σ_{10}, σ_{30}, and σ_{50}, respectively. This indicates that the power–law behavior extends to larger strain ranges, up to at least 50%, well beyond the range in strain that is considered for the E-modulus calculation (3–5% in this study).

2.4.4. Reversible versus Irreversible Densification

Figure 8 compares the compression curves of different density aerogels compressed to a given maximum strain value (20%, 35%, and 60%±5%) to better illustrate the extent of strain recovery as a function of density. The solid markers, plotted for each of the compression curves, represents the long-term relaxation derived from measuring the sample height 1 week after the compression test. Nearly all curves display a hysteresis between the compression and decompression curves, but the strain recovery after decompression and relaxation strongly depends on aerogel density/silica concentration. Samples compressed to a maximum strain of 20% (Figure 8a) recover between 6% and 20% of the absolute strain (i.e., 30–100% relative), with (near) full strain recovery for the intermediate-density aerogels. Aerogels
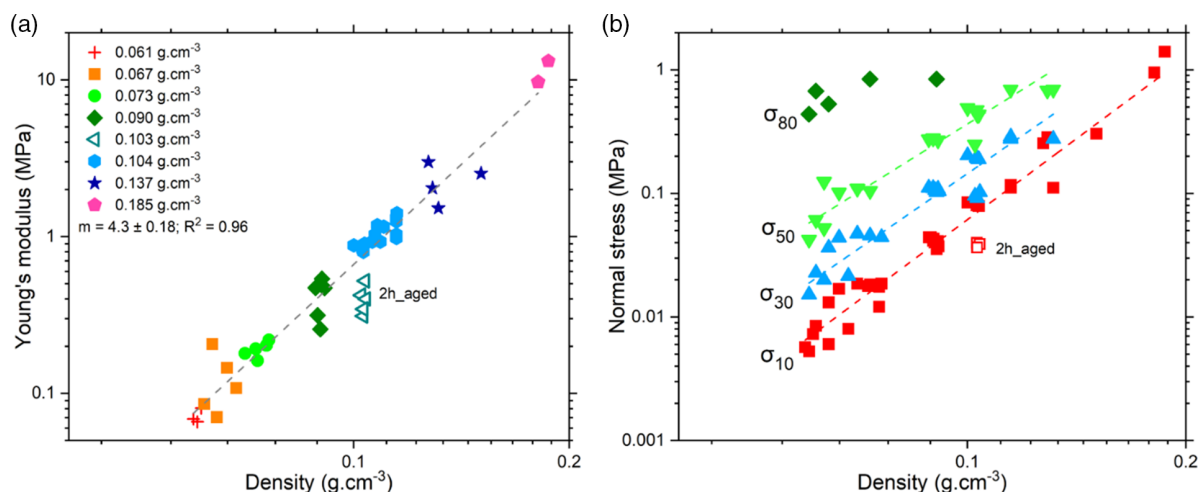

Figure 7. a) Elastic modulus as a function of initial aerogel density (set 1, 24 h aging). b) Normal stress at 10%, 30%, 50%, and 80% strain as a function of initial aerogel density (set 1, 24 h aging).
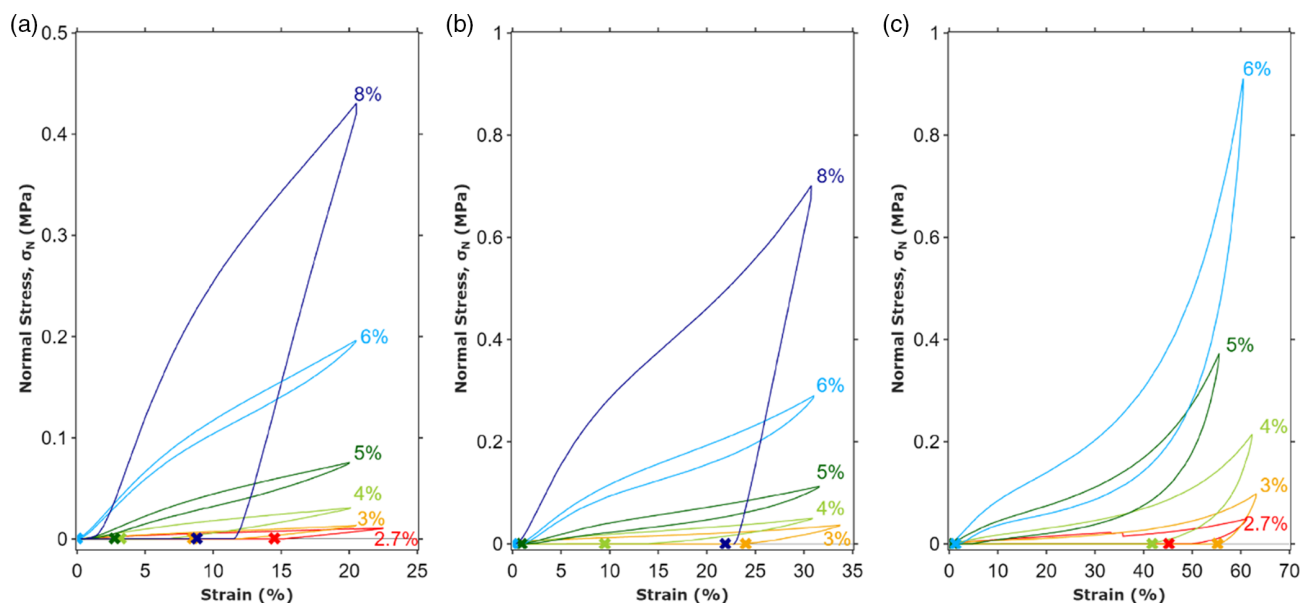
Figure 8. Compression–decompression data for different silica concentrations for a maximum strain of a) 20%, b) 35%, and c) 60 ± 5% maximum strain (set 1, 24 h aging). The values next to the curves correspond to the wt% silica in the sol. The crosses denote the strain 1 week after the measurement was completed. Note that, the plotted range in stress is half for (a) compared with (b,c).

compressed to a maximum strain of 30% (Figure 8b) recover between 6% and 30% of the absolute strain (i.e., 20–100% relative strain recovery), again with (near) full strain recovery for the intermediate density aerogels. Aerogels compressed to a maximum strain of 60% (Figure 8b) recover between 5% and 60% of the absolute strain (i.e., 8–100% relative), again with (near) full strain recovery for the intermediate density aerogels.

In other words, low-density aerogels display some degree of strain recovery when the compression was limited to relatively low strain values (50–70% relative strain recovery for up to 20% strain), but show a high degree of permanent densification after compression to higher strain values. In stark contrast, intermediate-density aerogels recover most of the strain after decompression, regardless of the maximum strain (up to maximum of 60% of compression, after which failure occurs). Higher-density aerogels are brittle and fracture at too low strain values to provide an accurate estimate of the strain recovery (Figure 5). One exception was a single cylinder of the 0.137 g cm^{-3} density series of aerogels, which did not fracture at 20% strain. Somewhat surprisingly, this sample displayed a rather poor strain recovery compared with the intermediate density samples. One possible explanation could be that minor fractures or sample buckling did occur, but without an easily identifiable fracture of the sample. In each case, given that this sample was more of the exception, rather than the rule in terms of fracture strain, its results should not be over-interpreted.

Figure 9 visualizes the strain recovery (taken from the relaxation of the cylinder height after 1 week) as a function of the maximum strain during the compression test for different aerogel densities (Figures 9a, S4, Supporting Information) and different aging times (Figures 9b, S3, Supporting Information). These data confirm the qualitative observations based on Figure 8. Low-density aerogels exhibit low strain recovery, particularly

for maximum strain values above 30%. Intermediate-density aerogels display near perfect strain recovery over the entire maximum strain range between 20% and 65%. High-density aerogels can only be investigated at low maximum strain because of their brittleness, but tend to display rather poor strain recovery. The effect of aging on strain recovery is also pronounced (Figure 9b): the intermediate density, 24 h-aged aerogel displays near perfect strain recovery, but a 2 h-aged aerogel of similar density recovers only half of the maximum strain, particularly for high maximum strain values. Thus, also in terms of strain recovery, the shorter-aged sample has a mechanical response that is typical for a lower density than its actual density.

3. Discussion

The mechanical properties of silica aerogels are determined by their density and aging conditions. To better discuss various mechanical responses and correlate them to aerogel spring back, it is easiest to group the materials into compressible (low density with short or long aging, intermediate density with short aging), viscoelastic (intermediate density with long aging times) and brittle (high density) regimes. Viscoelastic silica aerogels require intermediate densities and sufficiently long-term aging, but under these conditions can display a remarkable, near perfect strain recovery over a very wide range in strain (up to 65%). High-density aerogels are brittle, irrespective of the aging time (**Figure 10**a).

At intermediate silica concentrations, viscoelastic aerogels are obtained through the mechanical reinforcement provided by dissolution–precipitation processes during aging.[68] Increased aging enables transport of silica to weaker sections of the aerogels and the interparticle necks in particular,[35] which does
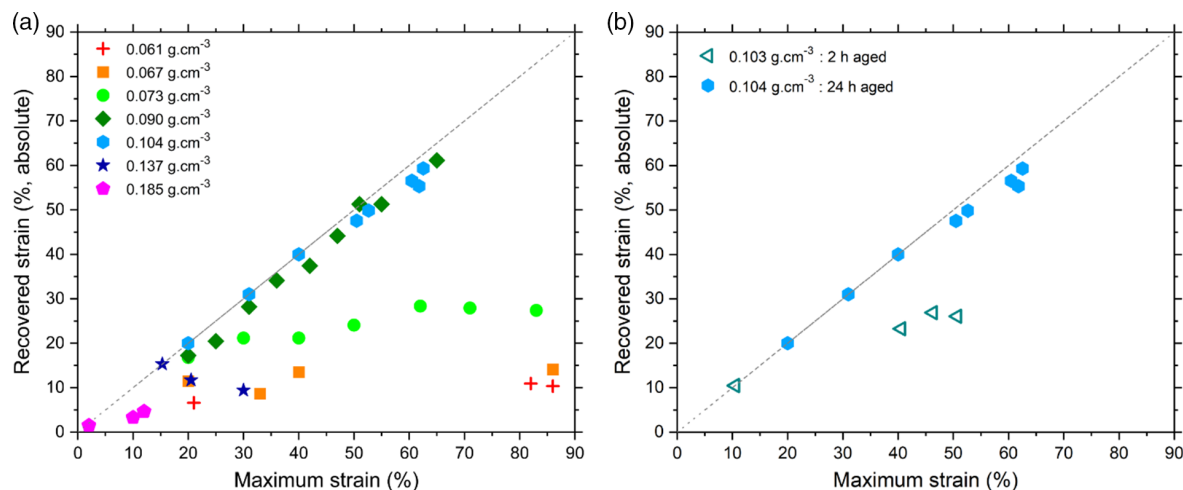
Figure 9. Absolute recovered strain as a function of maximum strain (set 1): a) for variable density for a constant aging time (24 h); b) for variable aging times (2 and 24 h) for a fixed silica concentration and density (6 wt%, 0.104 g/cm^3). The dotted 1:1 line corresponds to full strain recovery.

increase primary particle size and strength but does not change the geometry. This precipitated silica contributes to an increase in primary particle and cluster size and reduced specific surface area, and mean pore size.[37,38,69,70]

The density and aging time dependence of the APD induced shrinkage closely track the density and aging time dependence of the mechanical properties of the SCD aerogels. High silica concentrations and long aging times promote strain recovery of SCD aerogels, as well as aerogel spring back during APD (Figure 10b). Thus, the increases in stiffness and strength provided by higher silica concentrations and longer aging times promote aerogel spring back during APD and directly reduce APD shrinkage.[71,72] The APD density data (Figure 4, 10c) indicate a required minimum silica content to provide the necessary structural rigidity for withstanding the APD process without shrinkage.[73] In addition, sufficient aging is also important to limit APD shrinkage, particularly for the intermediate concentrations

near the density minimum (6 wt%) and high APD densities for shorter aging time in this silica concentration range. The same effect of aging is seen on the strain recovery of intermediate density aerogels. At low silica concentration, increased aging time also reduce APD shrinkage, but not enough to enable the synthesis of low-density aerogels.

The effects of silica concentration and aging on gel mechanics and aerogel spring back are not just academic. Commercial silica aerogels, whether produced by APD or SCD, typically have densities around 0.120 g cm^{-3}, in part because this is the density range where thermal conductivity is minimal[1,43,74,75] and in part because this density presents a reasonable compromise between mechanical strength and raw materials cost. Note that, this density is close to the lowest APD density that can be obtained with the current synthesis procedure, and requires both intermediate silica concentration and sufficiently long aging to ensure aerogel spring back. In fact, the silica concentrations required for APD
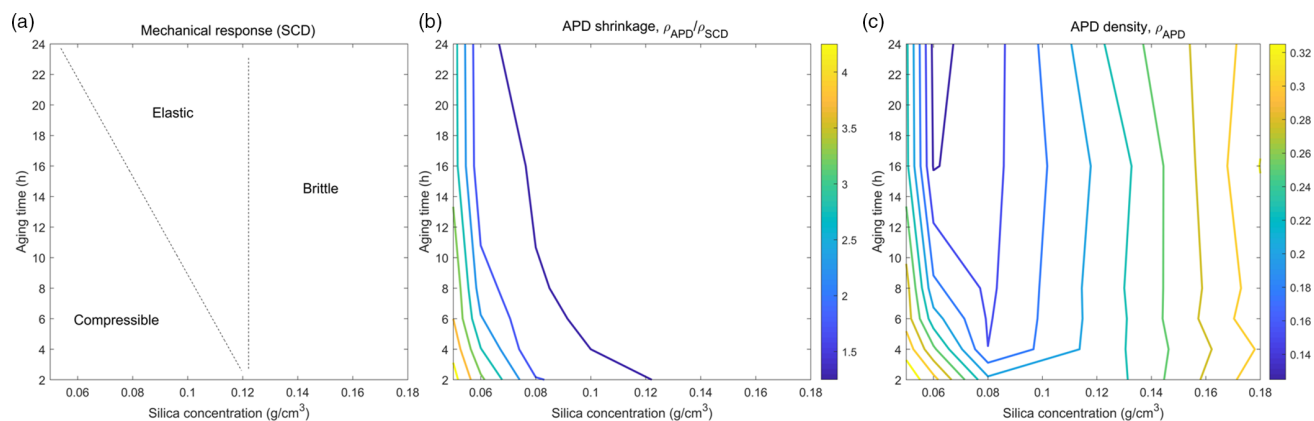

Figure 10. Effect of gel mechanics on APD shrinkage and density as a function of silica sol concentration and aging time. a) Different compressive regimes. b) APD shrinkage, contours drawn at ρ_{APD}/ρ_{SCD} linear intervals between 1.25 and 4.25 with a 0.50 step. c) APD density, contours drawn at linear intervals between 0.125 and 0.300 g cm^{-3} with a 0.025 g cm^{-3} step. Note that, the actual positions of the contours in (b,c) depend on the specific formulation and process conditions, but their general appearance and the qualitative conclusions drawn from them are applicable to other silica aerogel formulations.

aerogels of this intermediate density are only just above the cut-off point below which APD shrinkage cannot be avoided. From a cost perspective, the production of lower-density silica aerogels could be an attractive proposition. Our data indicate however that aerogels with low densities are not trivial to produce by APD. With the current protocol, for example, the lowest attainable APD density was on the order of $0.110 \, \mathrm{g \, cm^{-3}}$ and the production of APD silica aerogels of much lower density would require substantial optimization of the synthesis procedure (gelation, aging, hydrophobization, and drying conditions).

4. Conclusions

The study highlights the importance of various factors to be considered during APD and SCD for aerogel processing. Several polyethoxydisiloxane (PEDS)-based silica aerogels were produced using a two-step acid-base sol–gel process as a function of silica concentration and aging time. As expected, the SCD aerogel densities only depend on silica concentrations and not on aging conditions, and therefore closely track the expected theoretical values based on the solid content in the sol. In contrast, the APD aerogel densities display a more complex dependence on silica concentration and aging time, the lowest APD densities are reached at intermediate density ranges due to the interplay between aerogel spring back and solid content in the sol. The spring back during APD was found to closely track the strain recovery observed during uniaxial compression experiments on SCD reference aerogels: 1) limited strain recovery and high APD shrinkage at low silica concentrations, irrespective of aging time, 2) limited strain recovery and high APD shrinkage at intermediate silica concentrations and short aging times, 3) near complete strain recovery and negligible APD shrinkage at intermediate concentrations and long aging times, and 4) good strain recovery and negligible APD shrinkage at high silica concentrations, irrespective of aging time. The strong APD shrinkage at low silica concentrations places lower bounds on the density that can be achieved by APD. Analysis of strain recovery of aerogels produced by SCD provides critical information of the potential for APD of a particular material system.

5. Experimental Section

Materials: The silica source was either TEOS (Sigma Aldrich), or a prehydrolyzed form of TEOS with a SiO_2 equivalent silica concentration of 40 wt% (Dynasilan 40, Evonik). Denatured ethanol (95% ethanol/5% 1-propanol v/v%) was sourced from Alcosuisse AG. Nitric acid (70 wt%) and ammonia (28–30 v/v% in water) were acquired from Sigma Aldrich. Hexamethyldisiloxane (HMDSO, 99%) was acquired from Wacker Chemie and hydrochloric acid (HCl; 35.5–38% v/v% in water) was sourced from abcr swiss AG. Polystyrene molds for sample preparation were bought from Semadeni (article no. 1698).

Aerogel Synthesis: The preparation of a prehydrolyzed PEDS SP with a 20 wt% SiO_2 equivalent silica concentration was based on the procedure developed by Pajonk.[76] Briefly, 345.6 g of Dynasilan 40 (samples referred to as set 1) or an equivalent amount of TEOS (samples referred to as set 2) was transferred to a 1 L Schott bottle. Ethanol (153.55 g) and distilled water (54.4 g) were added to initiate hydrolysis. This solution was stirred rigorously for 5 min using a magnetic stirrer. To promote hydrolysis, 0.11 g of nitric acid was added separately to 153.55 g of ethanol. This solution was added drop by drop to the Dynasilan–ethanol–water mixture under constant mixing using a magnetic stirrer. After addition, the solution was kept at room temperature for half an hour, and subsequently stored at 10 °C overnight (**Figure 11**).

Different quantities of the SP were mixed with of ethanol to tune the silica content between 3 and 18 wt%. To 30 mL of the diluted ethanolic SP solution, 1 mL of water was added, along with increasing amounts of 5.5 M ammonia, proportional to the silica content (Table S1, Supporting Information). This gelation activated sol was stirred for 15–20 s and ≈5 mL aliquots were transferred into cylindrical molds, capped, and kept to age at 65 °C for variable aging times (standard condition 24 h, unless stated otherwise). The alcogels had dimensions of 13–15 mm in diameter and 17–23 mm in height. These alcogels were placed in a hydrophobization solution of 60 mL HMDSO, 2.5 mL ethanol, and 1.2 mL HCl at 65 °C for 24 h. The hydrophobized gels of set 1 were subsequently washed with ethanol and stored in ethanol for 24 h. The hydrophobized gels of set 2 were dried directly from the hydrophobization mixture without washing. Part of the gels were dried by APD: three cylinders were placed a crystalizing beaker in a preheated oven at 150 °C for 2 h. Other gels were dried by SCD, in a 500 mL autoclave (Separex, France) at 120 bar and 50 °C after 5 h of 10 g min^{-1} CO_2 circulation with continuous solvent extraction. As is clear from the earlier description, two sets of samples were part of this study: set 1 prepared by D. Sivaraman (2018–2020) and set 2 prepared by S. Iswar (2017). Both sets of samples were synthesized with a very similar protocol and the results were generally consistent. Small differences may arise from the use of TEOS versus Dynasilan-40 as the silica source,
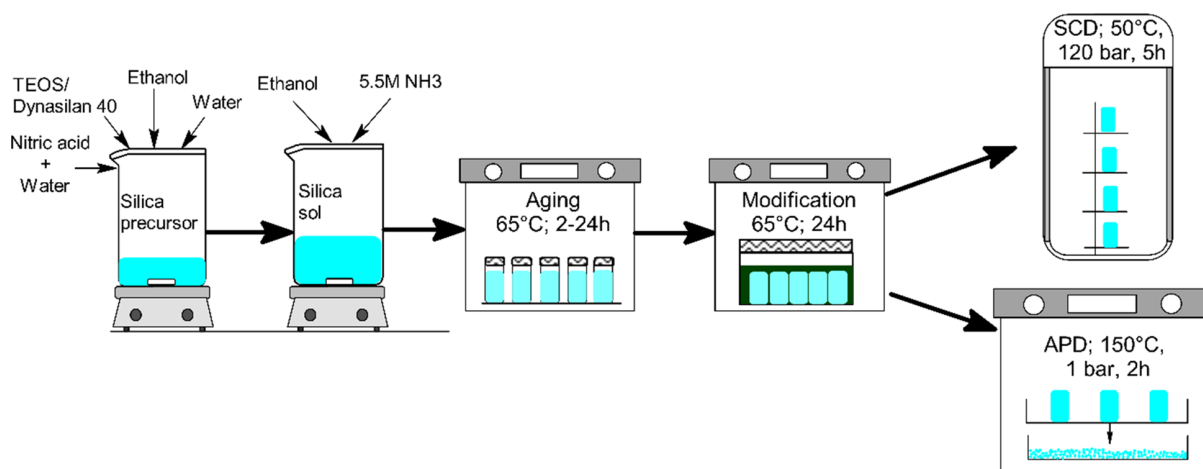

Figure 11. Synthesis scheme for aerogels.

or the presence (set 1) or absence (set 2) of an ethanol washing step after hydrophobization.

Characterization: The envelope density was analyzed by powder pycnometry (Micromeritics Geopyc 1360) on three ≈4 mm pieces of aerogel per measurement. The accuracy of measurement was estimated at 5%. The density of the SCD samples was determined from the mass and volume measured using calipers.

The surface area (S_{BET}) and pore structure were characterized by nitrogen sorption analysis. A sample (particle size ≈3 mm) of measured mass (typically ≈100 mg) was placed in a glass tube and degassed under vacuum to a pressure of 0.016 mbar for 20 h at 100 °C (heating rate of 10 °C min^{-1}). The samples were weighed again and the nitrogen sorption isotherms analyzed in a Micromeritics 3Flex instrument with P/P_0 ranging from 0.001 to 0.998 in 30 steps, equilibration times of 10 s for each incremental nitrogen addition, a minimum of 600 s per incremental step, leading to a total run time of ≈20 h. The analysis used the BET model to extract the surface area S_{BET}[45] and the BJH model to estimate mesopore volume and diameter.[48] Note that, pore size determinations of silica aerogels by nitrogen sorption analysis were incomplete: only samples pores below ≈50 nm in diameter were sampled, and complications arise from sample deformations during nitrogen sorption (capillary forces). Pore volume (V_{pore}) and average pore diameter (D_{pore}) were therefore also estimated from the envelope and skeletal density ($\rho_{envelope}$ and $\rho_{skeletal}$, respectively) and surface area, assuming a skeletal density of 2.0 g cm^{-3} and surface area assuming cylindrical pores.[77]

$$V_{pore} = \frac{1}{\rho_{envelope}} - \frac{1}{\rho_{skeletal}} \tag{1}$$

$$D_{pore} = \frac{4 \times V_{pore}}{S_{BET}} \tag{2}$$

Scanning electron microscopy (SEM) images were obtained using a FEI Nova NanoSEM 230 instrument (FEI, Hillsboro, Oregon, USA) at an accelerating voltage of 7 kV and a working distance of 4 mm. The aerogels were loaded onto the sample holder with a carbon tape and coated with 10–15 nm of platinum for imaging. Note that, this thickness corresponded to the thickness measured on the piezo detector during coating. The actual thickness of the coating on the aerogel was much lower due to the aerogel's extreme topography. Sample images were compiled using ImageJ open-source software.

Uniaxial compression tests were carried out on monolithic cylindrical samples (sanded to render plane parallel) using a universal materials testing machine (Zwick/Z010, Zwick/Roell, Germany) equipped with a 2 kN force transducer cell (KAP-S, AST Gruppe GmbH, Germany) in a controlled environment (temperature = 23 °C; relative humidity = 50 ± 5%). The compression rate was 1 mm min^{-1} until a variable, predefined strain value, followed by a slower decompression rate of 0.2 mm min^{-1}. Despite the relatively slow decompression rate, many samples displayed additional strain recovery after the decompression step was completed, which was quantified by measuring the height of the cylinders after 7 days. Nearly all samples displayed a hysteresis loop. The elastic moduli were calculated from the slope of the initial linear phase (3–5% strain) of the compression curve.[78]

Supporting Information

Supporting Information is available from the Wiley Online Library or from the author.

Conflict of Interest

The authors declare no conflict of interest.

Data Availability Statement

The data that support the findings of this study are openly available in polybox at https://polybox.ethz.ch/index.php/s/k6szTkQJd9zVlWw, in the data availability statement.

[1] N. Hüsing, U. Schubert, *Angew. Chem., Int. Ed.* **1998**, *37*, 22.

[2] R. Baetens, B. P. Jelle, A. Gustavsen, *Energy Build.* **2011**, *43*, 761.

[3] M. Koebel, A. Rigacci, P. Achard, *J. Sol-Gel Sci. Technol.* **2012**, *63*, 315.

[4] S. B. Riffat, G. Qiu, *Int. J. Low-Carbon Technol.* **2013**, *8*, 1.

[5] M. Schneider, A. Baiker, *Catal. Rev.* **1995**, *37*, 515.

[6] I. Smirnova, S. Suttiruengwong, W. Arlt, *J. Non-Cryst. Solids* **2004**, *350*, 54.

[7] R. W. Pekala, S. T. Mayer, J. L. Kaschmitter, F. M. Kong, *Carbon Aerogels: An Update on Structure, Properties, and Applications*, Lawrence Livermore National Lab., Livermore, CA **1993**.

[8] S. Zhao, G. Siqueira, S. Drdova, D. Norris, C. Ubert, A. Bonnin, S. Galmarini, M. Ganobjak, Z. Pan, S. Brunner, G. Nyström, J. Wang, M. M. Koebel, W. J. Malfait, *Nature* **2020**, *584*, 387.

[9] E. Cuce, P. M. Cuce, C. J. Wood, S. B. Riffat, *Renew. Sustain. Energy Rev.* **2014**, *34*, 273.

[10] Y. K. Li, D.-K. Yang, Y.-C. Chen, H.-J. Su, J.-C. Wu, Y. W. Chen-Yang, *Acta Biomater.* **2010**, *6*, 1462.

[11] M. Schmidt, F. Schwertfeger, *J. Non-Cryst. Solids* **1998**, *225*, 364.

[12] C.-T. Wang, C.-L. Wu, I.-C. Chen, Y.-H. Huang, *Sens. Actuators, B* **2005**, *107*, 402.

[13] P. J. Davis, C. Jeffrey Brinker, D. M. Smith, *J. Non-Cryst. Solids* **1992**, *142*, 189.

[14] H. Yokogawa, M. Yokoyama, *J. Non-Cryst. Solids* **1995**, *186*, 23.

[15] C. A. García-González, M. C. Camino-Rey, M. Alnaief, C. Zetzl, I. Smirnova, *J. Supercrit. Fluids* **2012**, *66*, 297.

[16] M. A. B. Meador, L. A. Capadona, L. McCorkle, D. S. Papadopoulos, N. Leventis, *Chem. Mater.* **2007**, *19*, 2247.

[17] S. Iswar, S. Galmarini, L. Bonanomi, J. Wernery, E. Roumeli, S. Nimalshantha, A. M. B. Ishai, M. Lattuada, M. M. Koebel, W. J. Malfait, *Acta Mater.* **2021**, 116959.

[18] N. Leventis, C. Sotiriou-Leventis, G. Zhang, A.-M. M. Rawashdeh, *Nano Lett.* **2002**, *2*, 957.

[19] M. A. B. Meador, S. L. Vivod, L. McCorkle, D. Quade, R. M. Sullivan, L. J. Ghosn, N. Clark, L. A. Capadona, *J. Mater. Chem.* **2008**, *18*, 1843.

[20] J. C. H. Wong, H. Kaymak, P. Tingaut, S. Brunner, M. M. Koebel, *Microporous Mesoporous Mater.* **2015**, *217*, 150.

[21] S. Zhao, W. J. Malfait, A. Demilecamps, Y. Zhang, S. Brunner, L. Huber, P. Tingaut, A. Rigacci, T. Budtova, M. M. Koebel, *Angew. Chem., Int. Ed.* **2015**, *127*, 14490.

[22] S. Zhao, Z. Zhang, G. Sèbe, R. Wu, R. V. R. Virtudazo, P. Tingaut, M. M. Koebel, *Adv. Funct. Mater.* **2015**, *25*, 2326.

[23] A. Venkateswara Rao, S. D. Bhagat, H. Hirashima, G. M. Pajonk, *J. Colloid Interface Sci.* **2006**, *300*, 279.

[24] G. Hayase, K. Kanamori, A. Maeno, K. Kaji, K. Nakanishi, *J. Non-Cryst. Solids* **2016**, *434*, 115.

[25] K. Kanamori, M. Aizawa, K. Nakanishi, T. Hanada, *Adv. Mater.* **2007**, *19*, 1589.

[26] G. Zu, T. Shimizu, K. Kanamori, Y. Zhu, A. Maeno, H. Kaji, J. Shen, K. Nakanishi, *ACS Nano* **2018**, *12*, 521.

[27] M. M. Koebel, L. Huber, S. Zhao, W. J. Malfait, *J. Sol-Gel Sci. Technol.* **2016**, *79*, 308.

[28] F. Shi, L. Wang, J. Liu, *Mater. Lett.* **2006**, *60*, 3718.

[29] P. R. Aravind, P. Shajesh, G. D. Soraru, K. G. K. Warrier, *J. Sol-Gel Sci. Technol.* **2010**, *54*, 105.

[30] S. S. Prakash, C. J. Brinker, A. J. Hurd, S. M. Rao, *Nature* **1995**, *374*, 439.

[31] A. P. Rao, A. V. Rao, G. M. Pajonk, *Appl. Surf. Sci.* **2007**, *253*, 6032.

[32] J. Wang, Z. S. Deng, J. Shen, L. Y. Chen, *J. Non-Cryst. Solids* **2000**, *271*, 100.

[33] R. Al-Oweini, H. El-Rassy, *J. Mol. Struct.* **2009**, *919*, 140.

[34] L. Huber, S. Zhao, W. J. Malfait, S. Vares, M. M. Koebel, *Angew. Chem., Int. Ed.* **2017**, *56*, 4753.

[35] P. B. Sarawade, J.-K. Kim, A. Hilonga, H. T. Kim, *Korean J. Chem. Eng.* **2010**, *27*, 1301.

[36] W. J. Malfait, S. Zhao, R. Verel, S. Iswar, D. Rentsch, R. Fener, Y. Zhang, B. Milow, M. M. Koebel, *Chem. Mater.* **2015**, *27*, 6737.

[37] S. Hæreid, E. Nilsen, M.-A. Einarsrud, *J. Non-Cryst. Solids* **1996**, *204*, 228.

[38] S. Iswar, W. J. Malfait, S. Balog, F. Winnefeld, M. Lattuada, M. M. Koebel, *Microporous Mesoporous Mater.* **2017**, *241*, 293.

[39] G. W. Scherer, *J. Non-Cryst. Solids* **1988**, *100*, 77.

[40] T. Woignier, J. Phalippou, *J. Phys. Colloq.* **1989**, *24*, C4.

[41] G. W. Scherer, *Cem. Concr. Res.* **1999**, *29*, 1149.

[42] A. Rigacci, M.-A. Einarsrud, E. Nilsen, R. Pirard, F. Ehrburger-Dolle, B. Chevalier, *J. Non-Cryst. Solids* **2004**, *350*, 196.

[43] J. C. H. Wong, H. Kaymak, S. Brunner, M. M. Koebel, *Microporous Mesoporous Mater.* **2014**, *183*, 23.

[44] G. M. Pajonk, E. Elaloui, P. Achard, B. Chevalier, J.-L. Chevalier, M. Durant, *J. Non-Cryst. Solids* **1995**, *186*, 1.

[45] S. Brunauer, P. H. Emmett, E. Teller, *J. Am. Chem. Soc.* **1938**, *60*, 309.

[46] J. L. Gurav, I.-K. Jung, H.-H. Park, E. S. Kang, D. Y. Nadargi, *J. Nanomater.* **2010**, *2010*, 1.

[47] M. Stolarski, J. Walendziewski, M. Steininger, Barbara Pniak, *Appl. Catal. Gen.* **1999**, *177*, 139.

[48] E. P. Barrett, L. G. Joyner, P. P. Halenda, *J. Am. Chem. Soc.* **1951**, *73*, 373.

[49] H. Tamon, T. Kitamura, M. Okazaki, *J. Colloid Interface Sci.* **1998**, *197*, 353.

[50] G. Reichenauer, G. W. Scherer, *J. Non-Cryst. Solids* **2001**, *285*, 167.

[51] A. Soleimani Dorcheh, M. H. Abbasi, *J. Mater. Process. Technol.* **2008**, *199*, 10.

[52] X. Zheng, H. Lee, T. H. Weisgraber, M. Shusteff, J. DeOtte, E. B. Duoss, J. D. Kuntz, M. M. Biener, Q. Ge, J. A. Jackson, S. O. Kucheyev, N. X. Fang, C. M. Spadaccini, *Science* **2014**, *344*, 1373.

[53] S. O. Kucheyev, M. Stadermann, S. J. Shin, J. H. Satcher, S. A. Gammon, S. A. Letts, T. van Buuren, A. V. Hamza, *Adv. Mater.* **2012**, *24*, 776.

[54] J. Majling, S. Komarneni, V. S. Fajnor, *J. Porous Mater.* **1995**, *1*, 91.

[55] G. W. Scherer, D. M. Smith, X. Qiu, J. M. Anderson, *J. Non-Cryst. Solids* **1995**, *186*, 316.

[56] L. Perin, A. Faivre, S. Calas-Etienne, T. Woignier, *J. Non-Cryst. Solids* **2004**, *333*, 68.

[57] J. S. Rivas Murillo, M. E. Bachlechner, F. A. Campo, E. J. Barbero, *J. Non-Cryst. Solids* **2010**, *356*, 1325.

[58] C. Sanchez-Valle, Z. A. D. Lethbridge, S. V. Sinogeikin, J. J. Williams, R. I. Walton, K. E. Evans, J. D. Bass, *J. Chem. Phys.* **2008**, *128*, 184503.

[59] A. Rege, M. Schestakow, I. Karadagli, L. Ratke, M. Itskov, *Soft Matter* **2016**, *12*, 7079.

[60] J. F. Poco, J. H. Satcher, L. W. Hrubesh, *J. Non-Cryst. Solids* **2001**, *285*, 57.

[61] S. Zhao, W. J. Malfait, N. Guerrero-Alburquerque, M. M. Koebel, G. Nyström, *Angew. Chem., Int. Ed.* **2018**, *57*, 7580.

[62] J. Groß, J. Fricke, *Nanostructured Mater.* **1995**, *6*, 905.

[63] T. Woignier, J. Reynes, A. Hafidi Alaoui, I. Beurroies, J. Phalippou, *J. Non-Cryst. Solids* **1998**, *241*, 45.

[64] R. Abdusalamov, C. Scherdel, M. Itskov, B. Milow, G. Reichenauer, A. Rege, *J. Phys. Chem. B* **2021**, *125*, 1944.

[65] R. W. Pekala, C. T. Alviso, J. D. LeMay, *J. Non-Cryst. Solids* **1990**, *125*, 67.

[66] S. Aney, J. Schettler, M. Schwan, B. Milow, A. Rege, *Adv. Eng. Mater.* **2021**, 2100095.

[67] K. E. Parmenter, F. Milstein, *J. Non-Cryst. Solids* **1998**, *223*, 179.

[68] F. Kirkbir, H. Murata, D. Meyers, S. R. Chaudhuri, *J. Non-Cryst. Solids* **1998**, *225*, 14.

[69] M.-A. Einarsrud, S. Haereid, *J. Sol-Gel Sci. Technol.* **1994**, *2*, 903.

[70] R. A. Strøm, Y. Masmoudi, A. Rigacci, G. Petermann, L. Gullberg, B. Chevalier, M.-A. Einarsrud, *J. Sol-Gel Sci. Technol.* **2007**, *41*, 291.

[71] C. J. Brinker, G. W. Scherer, *J. Non-Cryst. Solids* **1985**, *70*, 301.

[72] S. Smitha, P. Shajesh, P. R. Aravind, S. R. Kumar, P. K. Pillai, K. G. K. Warrier, *Microporous Mesoporous Mater.* **2006**, *91*, 286.

[73] K. Chou, B. I. Lee, *J. Mater. Sci.* **1994**, *29*, 3565.

[74] J. Fricke, X. Lu, P. Wang, D. Büttner, U. Heinemann, *Int. J. Heat Mass Transf.* **1992**, *35*, 2305.

[75] X. Lu, P. Wang, M. C. Arduini-Schuster, J. Kuhn, D. Büttner, O. Nilsson, U. Heinemann, J. Fricke, *J. Non-Cryst. Solids* **1992**, *145*, 207.

[76] G. M. Pajonk, *Colloid Polym. Sci.* **2003**, *281*, 637.

[77] A. Ayral, J. Phalippou, T. Woignier, *J. Mater. Sci.* **1992**, *27*, 1166.

[78] A. H. Alaoui, T. Woignier, G. W. Scherer, J. Phalippou, *J. Non-Cryst. Solids* **2008**, *354*, 4556.